Available online at www.sciencedirect.com

jmr&t Journal of Materials Research and Technology

journal homepage: www.elsevier.com/locate/jmrt

Original Article

Understanding the bending behavior and through-thickness strain distribution during asymmetrical rolling of high-strength aluminium alloy plates

Hui Su [a], Longgang Hou [a,b,*], Qingkun Tian [a], Yawen Wang [a], Linzhong Zhuang [c,d,**]

[a] State Key Laboratory for Advanced Metals and Materials, University of Science and Technology Beijing, Beijing 10083, China

[b] BCAST, Brunel University London, Kingston Lane, Uxbridge Middlesex UB8 3PH, United Kingdom

[c] Beijing Advanced Innovation Center for Materials Genome Engineering, University of Science and Technology Beijing, Beijing 10083, China

[d] Beijing Laboratory of Metallic Materials and Processing for Modern Transportation, University of Science and Technology Beijing, Beijing 10083, China

ARTICLE INFO

Article history:
Received 15 October 2022
Accepted 5 December 2022
Available online 9 December 2022

Keywords:
Asymmetric rolling
Finite element analysis
Deformation behavior
7050 aluminium alloy

ABSTRACT

The asymmetric rolling (ASR) process is highly desired to improve the through-thickness deformation/strain uniformity by introducing additional shear strains for uniform through-thickness microstructures and mechanical properties of metallic/alloy plates. In this study, the bending behavior and mechanism during the ASR processing of high-strength AA7050 aluminium alloy plates were simulated along with rolling trials. It shows that the plate will bend upward (toward slower roll) at larger speed ratios and smaller thickness reductions but downward (toward faster roll) at smaller speed ratios and larger thickness reductions. The ASR processing can increase the central equivalent plastic strains and decrease the surface-to-center strain gradient compared with that caused by the conventional symmetric rolling. The high strain rate bands (HSRBs) as key plastic strain accumulation regions are intimately connected with the post-rolling equivalent plastic strain distribution and the outgoing curvature. Especially, when the HSRB approaches the plate upper surface near the end of the deformation zone, normally at larger thickness reductions, a downward bending occurs despite that the lower roll rotates faster, and vice versa. The through-thickness HSRB induced by the ASR processing is considered to mainly enhancing the equivalent plastic strain homogeneity. The formation and interactive mechanisms of the HSRBs and their connection with the bending behavior during the ASR processing were discussed.

* Corresponding author.
** Corresponding author.
E-mail addresses: longgang.hou2@brunel.ac.uk, lghou@live.com (L. Hou), linzhongzhuang@163.com (L. Zhuang).

https://doi.org/10.1016/j.jmrt.2022.12.029

1. Introduction

Advanced aluminium alloy plates with high strength-to-weight ratio, good corrosion resistance and fracture toughness are usually manufactured by the conventional symmetric (hot) rolling (SR) process, which usually causes the surface-to-center plastic strain gradient, leading to ununiform microstructures and mechanical properties [1–3]. It is shown that the asymmetric rolling (ASR) process with different rotational speeds, roll diameters, or roll-to-plate friction conditions could cause intensive shear strains and accumulation of equivalent plastic strains inside the plates, consequently improving the through-thickness strain homogeneity compared with the SR process [4–8]. As a result, the ASR process has been widely applied for processing various metallic materials such as Mg [9–14], Al [15–20], Cu alloys [7,8,21], and other metallic materials [22–24], enabling the easy manufacture of large-scaled fine-grained materials comparing with other severe plastic deformation methods [25–28]. However, it also faces difficulties for rolling (mid)thick plates although it could benefit the microstructures and properties.

Firstly, the undesirable upward/downward bending issue depending on the ASR parameters will inhibit the next-pass plate biting and interrupt the rolling procedure, and even damage the rolling mill [29–31]. It was found that with different roll rotation speeds, the plate may be bent towards the slower roll at lower thickness reduction and the bending degree could be decreased by increasing the thickness reduction till bending towards the faster roll [32–34]. For rationalizing the outgoing curvature of the plates subjected to the ASR processing, the slab method and finite element method (FEM) are widely used. Qwamizadeh et al. [35] found that the bending was caused by the differences between the shear and axial strains in the upper and lower portions of each slab within the roll gap. Both strains have an opposite effect on the plate bending. The final curvature radius can be obtained by calculating the radius caused by the difference of the axial and/or shear strain. It was revealed that a higher reduction or larger initial plate thickness could facilitate to decrease the outgoing curvature and even change the bending direction. In addition, Cho et al. [12] found that the difference of shear strain rates between the upper and lower surfaces at the rolling biting zone strongly resulted in different outgoing curvatures under different rolling conditions. In general, the above-mentioned studies confirmed that the plastic strain during deformation could be closely related with the bending phenomenon.

Secondly, some studies showed that the ASR process can improve the through-thickness equivalent plastic strain homogeneity by effectively introducing shear strains into the plate center [6,36], i.e., the shear lines observed at the center layer of the ASR-ed plate [37–40]. However, different ASR parameters may complicate the deformation behavior and plastic strain distribution compared to that of the SR process. Furthermore, the plastic strain accumulation during the ASR processing that could reflect how the plastic strain (especially shear strain) could be effectively introduced into the plate center and reduced the plastic strain heterogeneity between the surface and plate center, was less concerned than the strain distribution in the rolled plate [1,6,41,42]. Actually, the ASR process can greatly affect the strain accumulation and the plate bending behavior, and thus to balance the through-thickness strain uniformity and the bending behavior, optimizing the key ASR parameters and in-depth mechanistic understanding are required for potential industrial trials.

For rolling thin sheets, it is easy to distinguish the upper and lower neutral points by comparing the surface flow speeds at the roll-contacting positions, and also the bending can be easily overcome by coiling tension. However, for rolling plates with larger initial thickness and high thickness reduction, especially without lubrication, the occurrence of sticking friction may cause problem for determining the neutral points [43,44]. Different rolling parameters may change the distribution of the neutral points, i.e., the neutral points at the upper or lower surface of the plate may even leave the deformation zone, inducing a more complex deformation zone configuration [45]. In addition, as the plate thickness increases, the plastic strain accumulation at the center layer becomes difficult and the enhanced surface-to-center strain gradient will lead to different through-thickness microstructures and mechanical properties [46,47]. In this study, the finite element method (FEM) and rolling trials were performed to reveal the deformation and bending behavior during the ASR processing of the (mid)thick AA7050 aluminium alloy plate. The plastic strain rate distribution, plastic strain accumulation and bending behavior during the ASR processing and their relationships were discussed.

2. Methods and experiments

The ASR process was simulated under plane strain condition by the MSC. MARC software with a 2-D model as illustrated in Fig. 1. The rolling parameters are listed in Table 1. The deformable plate was meshed with 1 mm element size while the work rolls and roll table were assumed as ideal rigid bodies. The materials data of AA7050 aluminium alloy and coulomb frictional condition (friction coefficient $\mu = 0.35$) were used [48]. The plates with 20 mm thickness were subjected to the ASR processing with 10–50% reduction and speed ratios between 1.0 (SR condition) and 1.6 achieved with a constant rotating speed (3 m/min) for the top roll and various rotating speeds (3–4.8 m/min) for the bottom roll. Totally, 35 rolling conditions were performed in the simulation. Five thickness layers (L = ±1 , ±0.5 and 0) and seven positions along rolling direction (RD) (number 0–6) were selected for deformation/strain analysis as illustrated in Fig. 1.

Supposing the coordinate of the curvature center as (x_c, y_c), three points (x_1, y_1), (x_2, y_2) and (x_3, y_3), were randomly collected at the lower (or upper) surface of the rolled plate, and the curvature radius (R) can be calculated by Eq. (1) [6,49],

$$\begin{cases} (x_1 - x_c)^2 + (y_1 - y_c)^2 = R^2 \\ (x_2 - x_c)^2 + (y_2 - y_c)^2 = R^2 \\ (x_3 - x_c)^2 + (y_3 - y_c)^2 = R^2 \\ |k| = 1/R \end{cases} \quad (1)$$

where the index $|k|$ is the reciprocal of the curvature radius, and smaller $|k|$ value corresponds to a relatively flat plate and

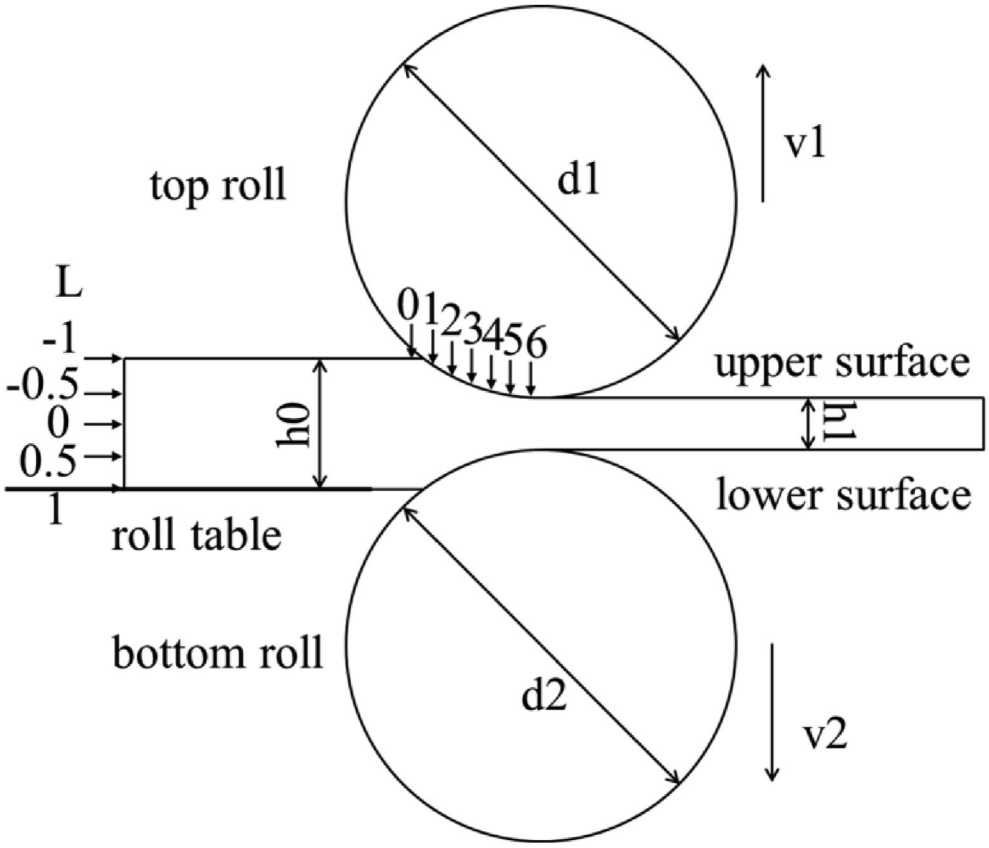

Fig. 1 – Schematic asymmetric rolling model. Five thickness positions: L = ± 1 for the lower/upper surface, L = ± 0.5 for the lower/upper quarter layer and L = 0 for the center layer. Number 0–6 represent different rolling stages from the biting zone to the exit).

will not exceed 0.005 because the present working roll radius is 200 mm. Note that the k value would be positive for the upward bending and negative for the downward bending, respectively.

The rolling experiments were carried out to verify the credibility of the simulation. AA7050 aluminium alloy plates (thickness: 20 mm) machined from a commercial 80 mm-thick plate were homogenized at 475 °C for 24 h with subsequently air cooling and rolled after holding at 400 °C for 1 h in an air furnace. The normal-rolling direction (ND-RD) plane was carved with grid lines to display the deformation during/after the rolling.

Table 1 – Rolling parameters for the simulation.

Parameter	Symbol	Value
Temperature (°C)	T	400
Friction coefficient	μ	0.35
Initial thickness (mm)	h_0	20
Final thickness (mm)	h_1	18,16,14,12,10
Normal thickness reduction (%)	Δh	10,20,30,40,50
Roll diameter (mm)	d_1, d_2	400
Speed ratio	i	1,1.1,1.2,1.3,1.4,1.5,1.6

3. Results

3.1. Curvature of the rolled plates

The calculated curvature index k under each rolling condition are decreased with thickness reduction (Δh, Fig. 2a), showing upward bending (towards slower roll) at small Δh value and downward bending (towards faster roll) at larger Δh value, which reveals an upward-to-downward bending transition with increasing Δh value. However, increasing the speed ratio (i) causes opposite bending behavior. Additional simulations with i = 1.1, Δh = 15% and i = 1.2, Δh = 25% are conducted to verify the trend. Obviously, there is a "critical reduction" (Δh_{crit}) under each speed ratio that can suppress the bending or keep k close to 0. As shown in Fig. 2b, this Δh_{crit} value increases firstly and then keeps almost constant at larger speed ratios, which means that further increasing the speed ratios cannot effectively suppress the downward bending when Δh exceeds a certain value (~33% for the current simulation, also see section 4.2). Fig. 2c- f compares the results between the experiments and simulations, and the calculated curvature index k values are close (see values in Table 2) and the simulation should be reliable. Some surface cracks (ND-RD plane in Fig. 2c) may be related with the carved grid lines before rolling.

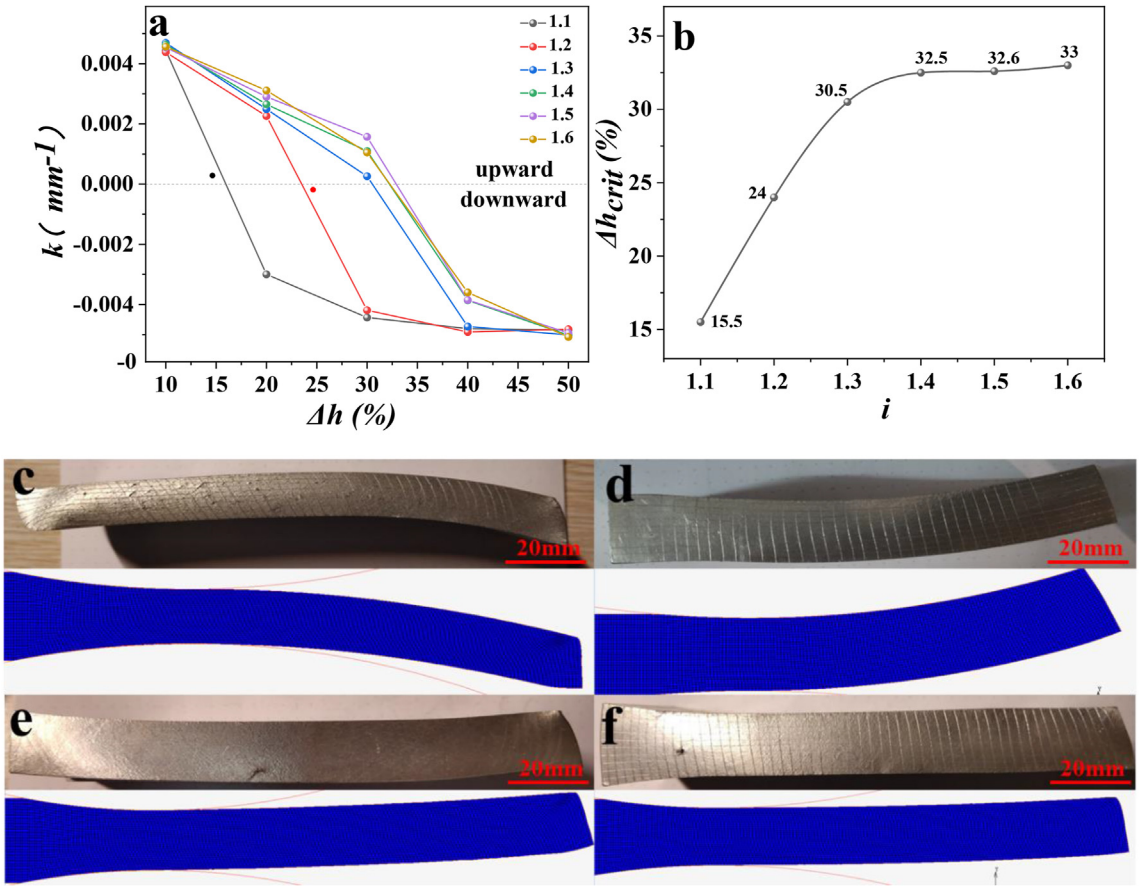

Fig. 2 – (a) Curvature index k values under different rolling conditions, (b) critical thickness reduction (Δh_{crit}) for different speed ratios and (c–f) comparison of rolling experiments and FEM results for the curvature and meshed lines: (c) i = 1.5, Δh = 40%, (d) i = 1.4, Δh = 10%, (e) i = 1.6, Δh = 30%, (f) i = 1.3, Δh = 30%.

3.2. *Equivalent plastic strain distribution and accumulation*

The equivalent plastic strain distributions after rolling along ND under different speed ratios (i) (Fig. 3a) show that increasing the speed ratios can promote the accumulation of the plastic strains at the center layer along with decreased through-thickness plastic strain discrepancy, which means an improved through-thickness homogeneity of the plastic strain distribution (see values in Table 3). Fig. 3b compares the equivalent plastic strain distributions between the ASR (solid lines) and SR (dotted lines) process es with same Δh value. It reveals that the total strain level mainly depends on the Δh value while the strain distribution along ND changes with the speed ratios. However, the plastic strain heterogeneity along ND is increased with Δh value.

To understand the equivalent plastic strain accumulation, the equivalent plastic strain distributions along ND at different rolling stages as marked in Fig. 1 for the SR and ASR processes are displayed in Fig. 3c and d, and the symmetric distribution relative to the center plane (L = 0) appears after the SR processing (Fig. 3c), while the asymmetric ones occur after the ASR processing (Fig. 3d). Nevertheless, the deformation is not uniformly accumulated along ND for both processes. For the SR process, the plastic strain accumulation mainly occurs near the surface layers at the start of the rolling (position 0 → 1) and then is gradually transferred inside the plate. At the end of the rolling (position 5 → 6), the plastic strain near the surface layer is slightly increased but without further accumulation inside the plate. Obviously, the equivalent plastic strains near the surface layer are mainly accumulated at three periods, i.e., position 0 → 1, 2 → 3, and 4 → 5, while it keeps increasing at the center layer after position 2. For the ASR process, as shown in Fig. 3d, at the biting region, the plastic strain accumulated near the lower surface is higher than that near the upper surface. As the rolling continues, the region with significantly accumulated plastic strains is

Table 2 – K values between the simulations and experiments in Fig. 2.

Index k ($\times 10^{-3}$/mm)	Rolling condition			
	i = 1.5, Δh = 40%	i = 1.4, Δh = 10%	i = 1.6, Δh = 30%	i = 1.3, Δh = 30%
Simulation	−3.84	4.48	1.05	0.31
Experiment	−3.71	4.21	0.96	0.24
Difference	0.13	0.27	0.09	0.07

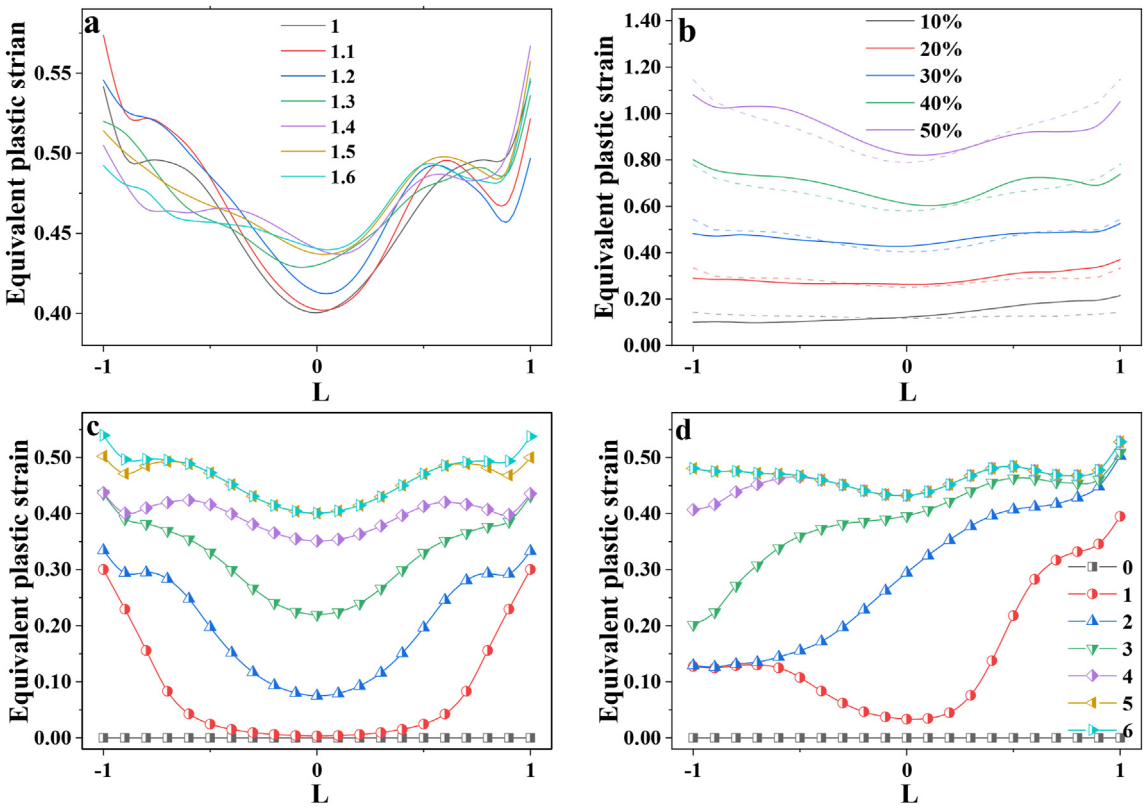

Fig. 3 – Equivalent plastic strain distributions along ND for (a) $\Delta h = 30\%$ with different speed ratios, (b) $i = 1.3$ with different thickness reductions (The dotted lines represent the SR conditions with same Δh value), (c) SR ($i = 1$, $\Delta h = 30\%$) and (d) ASR ($i = 1.3$, $\Delta h = 30\%$) at different rolling stages.

gradually moved upward. The deformation near the lower surface is mainly concentrated at the early stage (position 0 → 2) while the plastic strains near the upper surface are mainly accumulated at two periods, i.e., the position 0 → 1 and 2 → 5, apparently different from that of the SR process. Both two different plastic strain accumulation behavior can affect their final plastic strain distributions. For example, the ASR plate (0.44) exhibits ~10% higher plastic strain at the center layer than the SR plate (0.4) under same thickness reduction, thus decreasing the surface-to-center strain gradient.

Table 3 – Plastic strain differences between the surface and center layers after rolling with $\Delta h = 30\%$ and different speed ratios.

Rolling process	i	Equivalent plastic strain gradient	
		Upper surface → center	Lower surface → center
SR	1	0.14	0.14
ASR	1.1	0.17	0.10
	1.2	0.13	0.08
	1.3	0.09	0.10
	1.4	0.06	0.12
	1.5	0.08	0.12
	1.6	0.05	0.11

3.3. *Plastic strain rate distribution*

As confirmed in section 3.2, the equivalent plastic strain accumulation is ununiform during the rolling along either RD or ND. The plastic strains are mostly accumulated during a relatively narrow rolling stage (e.g., position 0 → 1 for the lower surface of the ASR condition), suggesting a higher plastic strain rate. As shown in Fig. 4, the band-like regions with high strain rate, namely high strain rate bands (HSRBs), are formed and obviously affected by rolling parameters. For the SR process ($i = 1$ in Fig. 4), the single '**X**' shaped HSRBs appear for $\Delta h < 20\%$ while the double '**X**' shaped HSRBs appear for $\Delta h \geq 30\%$. However, the HSRB distribution induced by the ASR process can be roughly divided into four types.

Type I: for $\Delta h = 10\%$ and $i = 1.1$–1.6 (within the red frame), the '**V**'-shaped HSRBs with low intensity appears in the early deformation stage.
Type II: for $\Delta h = 20$–30% (within the green frame), the HSRBs generated near the lower surface can go through the plate thickness, causing a '**Y**'-shaped HSRBs.

Type III: for the rolling conditions within the black frame, i.e., $i < 1.3$ with $\Delta h = 40\%$ or $i < 1.5$ with $\Delta h = 50\%$, the first '**X**'-shaped HSRB at the biting zone is similar to that of the SR process with same Δh but the second '**X**'-shaped HSRB for the SR process turns into a '**Y**'-shaped one.

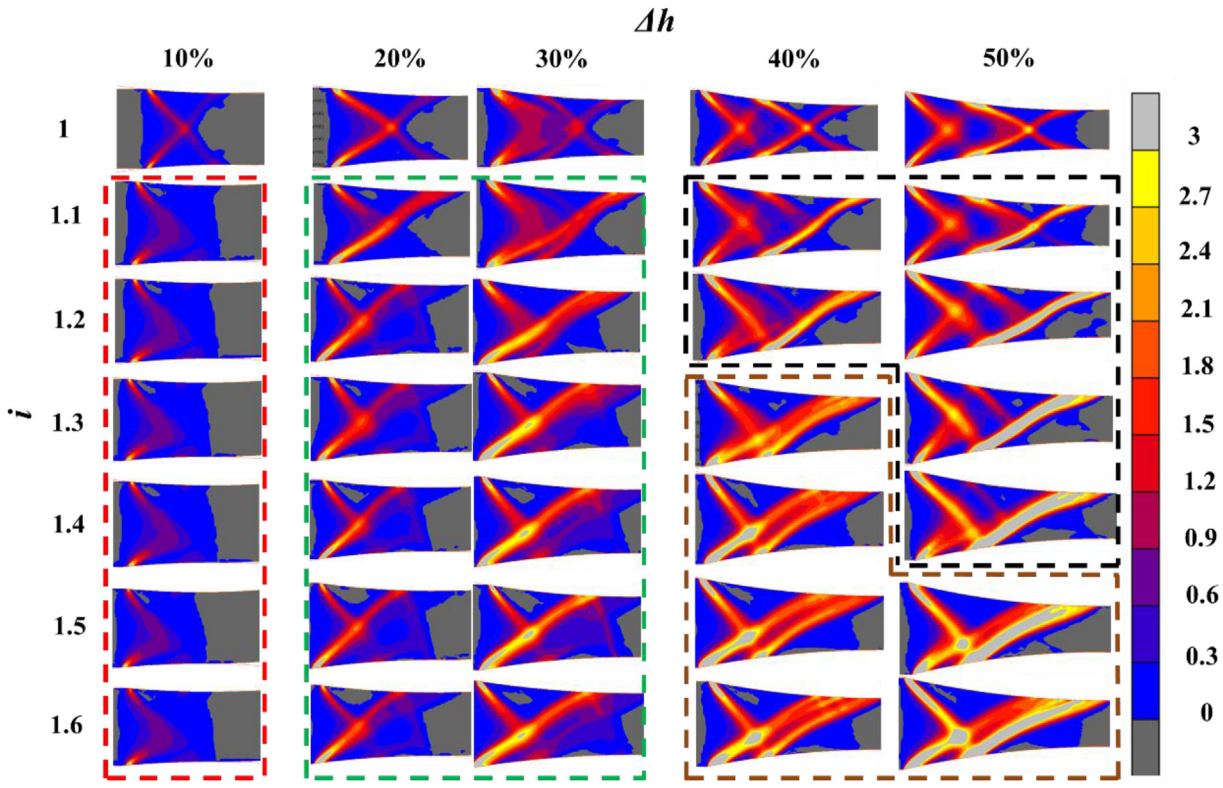

Fig. 4 – Equivalent plastic strain rate distribution under different rolling conditions.

Type IV: the '**Y**'-shaped HSRBs within the brown frame, i.e., $i > 1.2$ with $\Delta h = 40\%$ or $i > 1.4$ with $\Delta h = 50\%$, are similar to those in the green frame except that the merged through-thickness HSRB consists of two parallel HSRBs, and the right one is further enhanced at $\Delta h = 50\%$.

As can be seen from Fig. 4, the HSRB distributions are closely related to the rolling parameters and become complex at high Δh. Pawelski [50] found similar plastic strain rate distribution as type II and type III using the stationary FE method. The HSRB was considered to be distributed along 11 rigid triangles, which remained undeformed during rolling. Also, the similar HSRB distributions as type II and type III was also observed during the single roll-driven rolling [51]. The current simulation reveals more HSRB distributions (type I and type IV) under different rolling conditions, as well as the evolution of the HSRB distribution with rolling parameters.

3.4. *Plastic strain accumulated at HSRB*

The distributions of the plastic strain rate and plastic strain during the ASR processing with $i = 1.3$ and $\Delta h = 10–50\%$ in Fig. 5 indicate that the equivalent plastic strains in these HSRBs increase rapidly and dominate the plastic strain accumulation. For the low strain rate regions (LSRRs, blue areas in Fig. 5(a1-e1)), the equivalent plastic strain accumulation is less significant (Fig. 5(a2-e2)). Then, the equivalent plastic strain for each HSRB at the upper and lower surfaces is collected in Fig. 6. The ε_{u1}, ε_{u2}, ε_{u3} and ε_{l1}, ε_{l2}, ε_{l3} are the equivalent plastic strains accumulated at the 1st, 2nd and 3rd HSRBs from the biting zone at the upper and lower surfaces (Fig. 6f), respectively. Noticeably, the ε value should be zero if the HSRB disappears or does not exist. At the biting zone, both ε_{u1} and ε_{l1} are increased with Δh. As the speed ratio increases, the ε_{u1} decreases while the ε_{l1} is relatively stable, although the latter is higher under most ASR conditions ($\Delta h < 50\%$). The lower part of the plate is subjected to larger plastic strains as the bottom roll rotates faster. With increasing the Δh to 50% at $i = 1.1–1.4$, the ε_{u1} and ε_{l1} are similar because the deformation characteristics at the biting zone are similar to that of the SR process (Fig. 4). The ε_{u2} and ε_{l2} are roughly increased with Δh. For example, with $\Delta h = 50\%$, the ε_{u2} is higher at $i = 1.5–1.6$ but smaller at $i = 1.1–1.3$. It is of concern that for the rolling conditions within the yellow frame in Fig. 4, the second HSRB near the upper layer is composed of two parallel HSRBs, which can be merged when reaching the upper surface, making them difficult to be calculated individually and thus the ε_{u2} is highly increased under these conditions. The smaller values at $i = 1.1–1.3$ is due to a weaker HSRB in the center layer, which can be regarded as a partial reservation of the HSRB distribution under the SR condition. The ε_{u3} only exists at $i \leq 1.3$, while the ε_{l3} disappears in all ASR conditions. In general, it seems that the 1st HSRB can play a critical role in the strain accumulation when $\Delta h \leq 20\%$, and with $\Delta h > 30\%$, the plastic strain accumulation at the 2nd or 3rd HSRB is increased gradually and exceeds that accumulated at the 1st HSRB.

The ratio of the equivalent plastic strain accumulated at the HSRB relative to the total equivalent plastic strain is

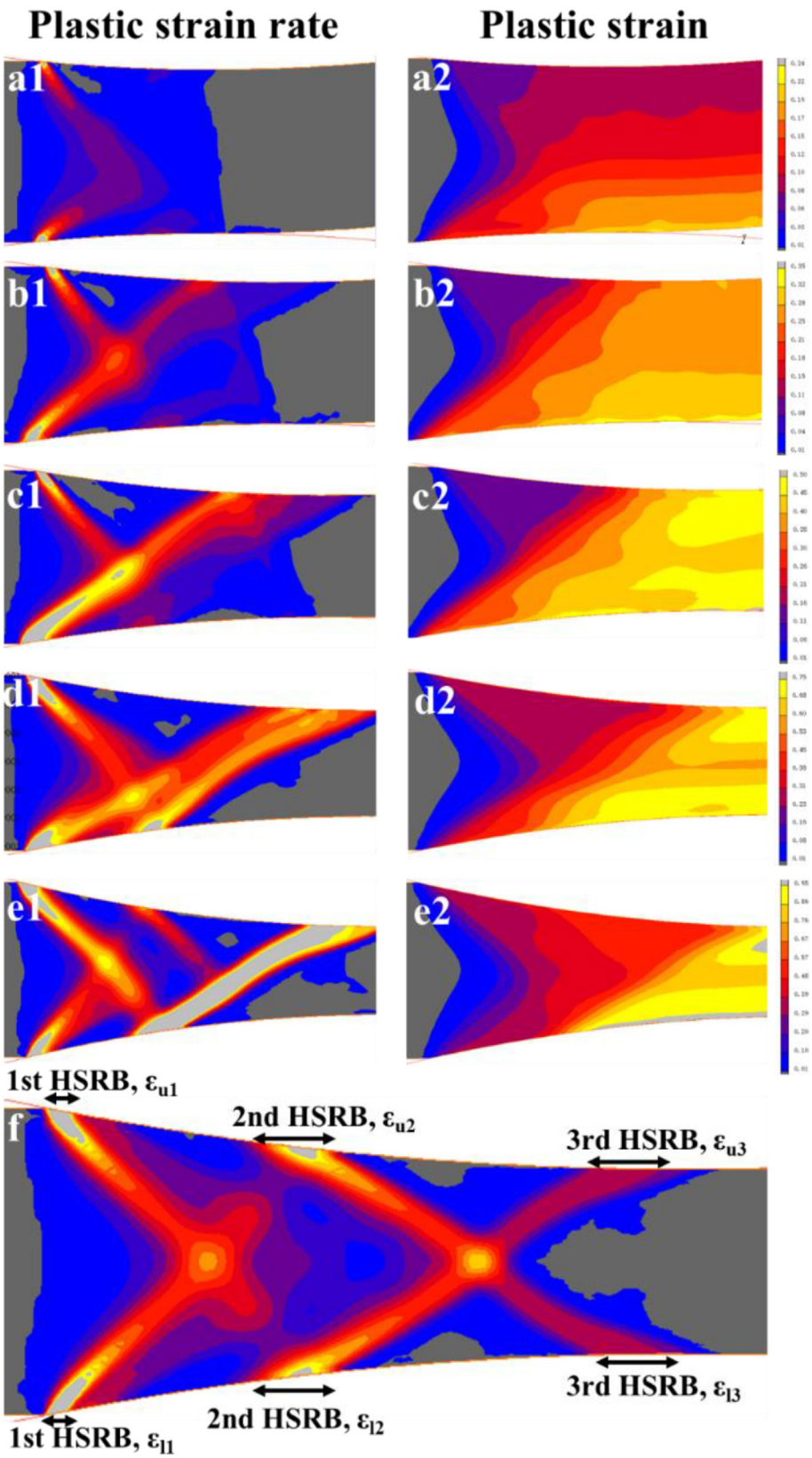

Fig. 5 – Comparison between the equivalent plastic strain rate distribution and equivalent plastic strain distribution during the ASR processing with i = 1.3 and different Δh values: (a) 10%, (b) 20%, (c) 30%, (d) 40%, (e) 50% and (f) sequence of the HSRBs.

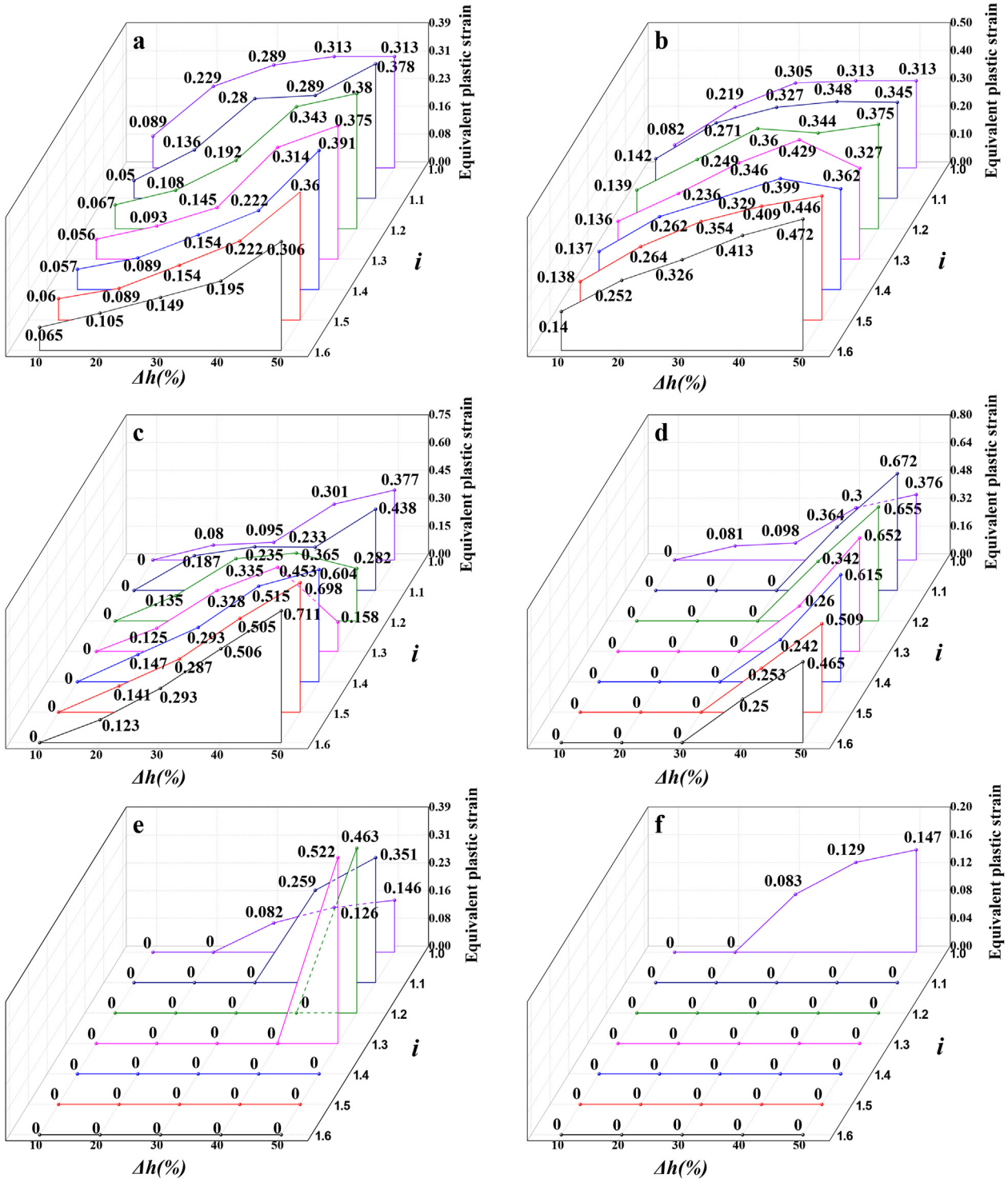

Fig. 6 – ε_u and ε_l values under different rolling conditions: (a) ε_{u1}; (b) ε_{l1}; (c) ε_{u2}; (d) ε_{l2}; (e) ε_{u3}; (f) ε_{l3}.

calculated by Eq. (2) to quantitatively reflect the plastic strain concentration, as shown in Fig. 7.

$$\begin{cases} E_u = \dfrac{\varepsilon_{u1} + \varepsilon_{u2} + \varepsilon_{u3}}{\varepsilon_u} \\ E_l = \dfrac{\varepsilon_{l1} + \varepsilon_{l2} + \varepsilon_{l3}}{\varepsilon_l} \end{cases} \quad (2)$$

Here, ε_u and ε_l are the equivalent plastic strains at the upper and lower surfaces, respectively. It shows that both E_u and E_l are generally increased with Δh except that E_l is decreased at $\Delta h = 30\%$ because a weak HSRB generated at the lower surface is not considered here (see Fig. 4). This weak HSRB will be enhanced at larger Δh, causing the second through-thickness HSRB and a higher E_l value. Fig. 7 confirms

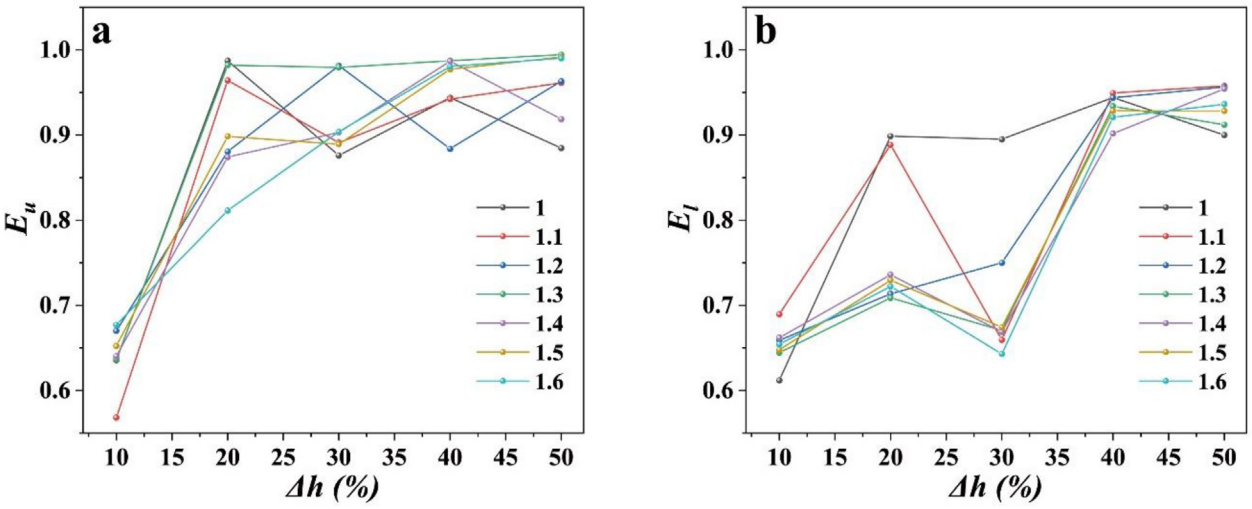

Fig. 7 – E_u (a) and E_l (b) values under different rolling conditions.

that most of the equivalent plastic strains are accumulated at HSRBs, especially for the ASR process with larger Δh value.

4. Discussion

Kasai et al. [51] observed the equivalent plastic strain rate distributions during single roll driven rolling for small and high Δh, which are similar to those in the green and black frames in Fig. 4. They also demonstrated that the accelerations of materials flow speed are closely related to the plastic strain rate by solving a series of equations. Section 3.4 shows that the HSRB is the main plastic strain accumulation region, and thus a significant acceleration change should occur when the materials pass through the HSRB during rolling. Based on the above inference, the local deformation inside the plate can be analyzed by the changes in the direction and the magnitude of the node acceleration at the corresponding position. Besides, during the stable rolling stage, the outgoing part of the plate may curve for most ASR conditions and a centripetal acceleration should appear correspondingly, which could help understanding the occurrence of the bending.

4.1. *HSRB formation and distribution*

Fig. 8 displays typical acceleration vectors for both SR and ASR processes and their distributions are highly coincident with the HSRB distributions under same rolling condition. This section focuses on the formation and interaction mechanism of the HSRBs and their effects to the bending behavior, and the plastic strain homogeneity will be discussed in section 4.2 and 4.3.

For the SR process with $\Delta h = 40\%$ (Fig. 8a), the HSRBs can be transferred from the surface to the center layers at the biting zone. Two HSRBs formed near the upper and lower surfaces interact with each other at the center plane and then their directions are changed towards the surfaces, causing the first '**X**'-shaped HSRB. Then, after reaching the surface layer, the first HSRB is enhanced by the roll compression and the second '**X**'-shaped HSRB is formed similarly. For a small thickness reduction, the decreased plastic strain rate cannot promote the interaction near the center plane and the plastic deformation zone is also shortened, which will weaken the second '**X**'-shaped HSRB or even lead to its disappearance.

For the ASR process, as shown in Fig. 8b–e, the HSRB distributions are changed and no longer symmetrically distributed with respect to the center plane, yet following similar rules as mentioned above for the SR process. As the speed mismatch is introduced, the first HSRB generated at the lower surface is intensified and more inclined than that generated at the upper surface. When these two HSRBs are interacted with each other near the center, the weaker one changes its direction while the stronger one partially maintains its direction, thus leading to the first through-thickness HSRB. Different rolling parameters could induce different HSRB distributions, as shown in Fig. 4.

Fig. 9 schematically illustrates the formation and interaction mechanism of the HSRBs, in which the deformation region is divided into the HSRBs and LSRRs according to the distribution of the equivalent plastic strain rate. Here, the HSRB along ND and RD directions is decomposed to simplify the description. The ND components of the HSRBs in the upper and lower surfaces are equal because of the symmetric rolling geometry (same roll diameter) and the RD components are different because of the different rotating speeds of the upper and bottom rolls. The ND components are symmetrically strengthened for the upper and lower surfaces when the Δh increases as the symmetric geometry remains unchanged during rolling. When the speed ratio is introduced, i.e., the circumferential speed of the bottom roll increases, on the other hand, the RD component at the lower surface is higher than that at the upper surface, making the first HSRB generated at the lower surface more inclined than that at the upper surface. However, the influences of speed ratios on the HSRB distribution are limited under some thickness reductions, which means further increasing the speed ratio cannot affect

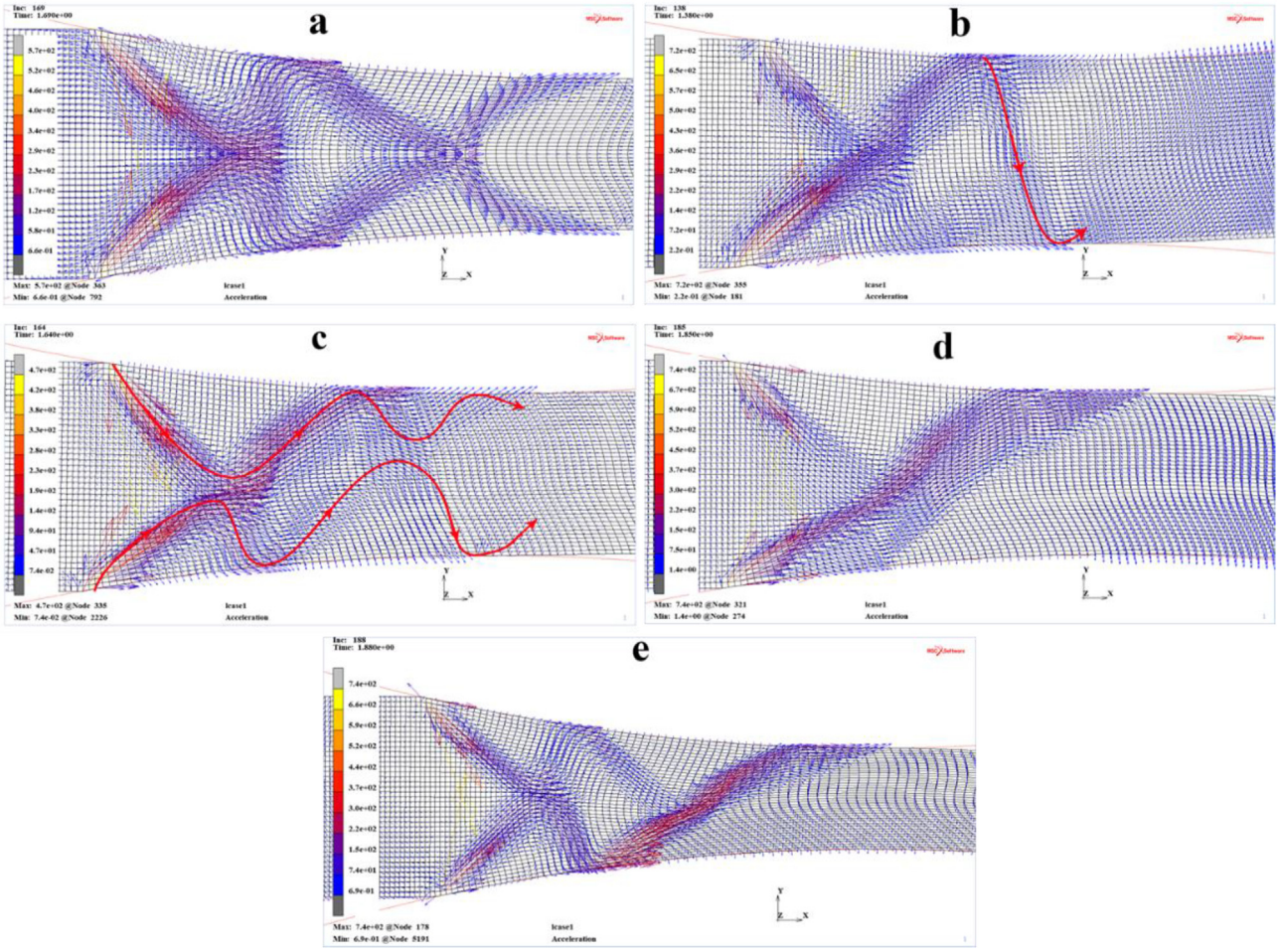

Fig. 8 – Typical acceleration vectors under different rolling conditions: (a) SR with $\Delta h = 40\%$ and (b–e) ASR with different bending behavior: (b) upward bending ($i = 1.4$, $\Delta h = 20\%$), (c) without obvious bending ($i = 1.3$, $\Delta h = 30\%$), (d) downward bending with small Δh ($i = 1.2$, $\Delta h = 30\%$) and (e) high Δh ($i = 1.3$, $\Delta h = 50\%$).

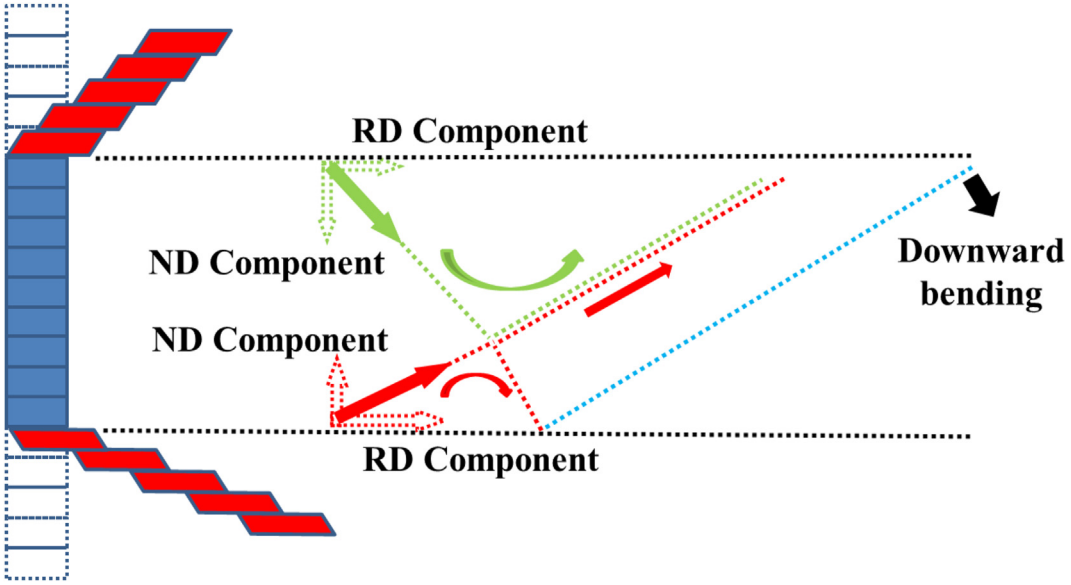

Fig. 9 – Schematic HSRB formation mechanism during the ASR processing.

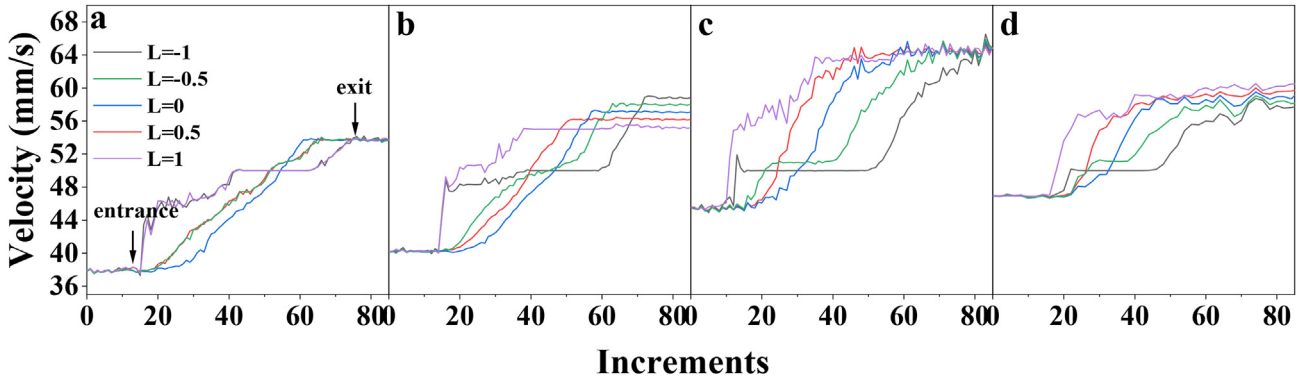

Fig. 10 – Material flow speeds along RD at different thickness positions under different rolling conditions: (a) SR: $i = 1$, $\Delta h = 30\%$, (b) downward bending: $i = 1.1$, $\Delta h = 30\%$, (c) flat: $i = 1.3$, $\Delta h = 30\%$, (d) upward bending: $i = 1.3$, $\Delta h = 20\%$.

the HSRB distribution when exceeding the limit, as shown in Fig. 4. This also can explain that the HSRB distribution at the rolling biting region is similar to that of the SR process when high Δh and small i are applied, i.e., the ND component of the HSRB plays a more critical role than the RD component. The upper and lower HSRBs generated at the rolling biting zone will interact at the center plane and then the upper HSRB (green-arrowed) will change its direction while part of the lower HSRB (red-arrowed) keeps its direction towards the upper surface, thus forming the first through-thickness HSRB (red- and green-dotted lines). Although most of the HSRBs transferred upwards, part of them will change their directions again after approaching the lower surface because of the support of the bottom roll, and the second through-thickness HSRB is formed (blue-dotted line). Furthermore, these two through-thickness HSRBs will merge into one wider and stronger HSRBs under some rolling conditions (i.e., the yellow frame in Fig. 5), converting the HSRBs in the opposite direction during the SR process.

Actually, the HSRBs distribution could be varied with rolling parameters and may not be same with that in Fig. 9. For example, in Fig. 4, for $\Delta h = 10\%$, the first through-thickness HSRB is not fully developed and only partial HSRBs transmit along the red- and green-dotted lines in Fig. 9, which leads to a '**V**'-shaped distribution. With increasing Δh from 20% to 30%, only the first through-thickness HSRB is well developed. For $\Delta h > 40\%$ and $i > 1.3$, a typical HSRB distribution in Fig. 9 can be found, and for the cases with $i < 1.3$ at the same Δh, the HSRB distribution in the SR process is partially retained. Although the HSRB distribution varies with rolling parameters, the deformation follows the same rule as discussed above.

4.2. *Materials flow and plate bending during rolling*

It can be known that increasing Δh can prevent the plate bending towards the slower roll (upward bending) and facilitate the downward bending during the ASR processing. Obviously, when the metal flow speed near the lower surface is higher than that near the upper surface, the plate will be bent upwards and vice versa [31,52]. This suggests that a larger Δh can increase the flow speed near the upper surface at the end of the deformation zone, even though the top roll rotates slower. Fig. 10 shows typical flow speed distribution at five thickness positions (see Fig. 1) under four typical rolling conditions including the SR process and ASR process with different bending behavior. The SR process has a symmetric flow speed distribution but an asymmetric for the ASR process with respect to the central plane. For the condition of $i = 1.1$ and $\Delta h = 30\%$, the upper layer shows a higher speed than the lower layer at the end of rolling (Fig. 10b). With increasing i to 1.3 (Fig. 10c), the flow speeds at these five positions are almost the same at the end of rolling, corresponding to a nearly flat shape (see Fig. 2f). However, for rolling with $i = 1.3$ and $\Delta h = 20\%$, the lower surface exhibits the highest flow speed at the exit (Fig. 10d), corresponding to an upward bending. It can be seen from Fig. 10 that the flow speeds at the surface layers are accelerated twice at the beginning and near the end of the deformation zone and equal to the circumferential speed of the contacting roll between the two rolling stages mentioned above, reflecting a sticking friction condition [43,53]. One noticeable difference between the upward and downward bending is that, the flow speed at the upper surface is higher at larger Δh, which finally causes downward bending. Comparing Figs. 4 and 10, one can find that the material flow speed is increased obviously when passing through the HSRBs, as confirmed in ref. [51]. If the last HSRB approaches the upper surface at the end of the deformation zone with sufficient intensity and no HSRB with the same magnitude appears on the opposite side, the plate will bend downwards. This signifies that the last HSRB at the upper surface plays a critical role in the plate bending, which seems not constant with Cho et al.'s finding [12] that the bending behavior could be associated with the shear strain rate difference between the upper and lower layers of the sheet (h_0: 5 mm, Δh: 10%). The shear strain gradient can be mainly determined in the biting region, consequently affecting the bending behavior. These different conclusions might be related to different rolling conditions. The thickness reduction of 10% used in ref. [12] is similar to the first column in Fig. 4, but the HSRBs are concentrated at the biting region, actually being consistent with our results.

Additionally, for rolling with $i = 1.3$ and $\Delta h = 20\%$ (Fig. 8b, i.e., upward bending), a weak HSRB is transferred downward near the end of the deformation zone and reaches the lower

surface at the end of the deformation zone, causing an upward bending. For rolling with $i = 1.3$ and $\Delta h = 30\%$ (Fig. 8c, i.e., no bending), as red-arrowed, the HSRB reaches both the upper and lower surfaces together near the end of the deformation zone, thus resulting in a nearly flat plate in the final. For rolling with $i = 1.2$ and $\Delta h = 30\%$ (Fig. 8d), a strong HSRB reaches the upper surface near the rolling exit and is resisted by the top roll, leading to a downward bending. However, as the Δh is relatively small, increasing the speed ratio can effectively suppress the downward bending (Fig. 10c). For rolling with $i = 1.3$ and $\Delta h = 50\%$ (Fig. 8e), as the Δh further increases, a strongly inclined HSRB appears along with a downward bending, which is difficult to be compensated by increasing the speed ratio.

Although the plastic strain accumulation and distribution play a critical role in plate bending [12,35], the bending behavior should be related to the changes of the external loads. The interaction between the work roll and the HSRB can result in different bending states under different rolling conditions. In general, the influence of the HSRBs on the plate bending can be described as follows: when the HSRB approaches the upper surface near the end of the deformation zone, the plastic strain will change its direction toward the lower surface because of the support from the top roll, resulting in a downward acceleration for the outgoing plate as well as downward bending. On the contrary, for the ASR processing with high i and small Δh, when the second HSRB approaches the upper surface and changes its direction earlier, there is still enough space for the last HSRB to arrive the bottom surface within the deformation zone, and the bottom roll still can suppress the downward bending, as shown in Fig. 4 for $i = 1.4–1.6$ and $\Delta h = 30\%$. Noticeably, for the rolling conditions within the brown frame in Fig. 4, with increasing Δh, the last HSRB will be closer to the end of the deformation zone, making it impossible to adjust downward bending by increasing the speed ratio. This also can explain that the effects of speed ratios are only valid within a specific range, and the Δh_{crit} that can effectively suppress the plate bending will not increase with the speed ratio after a specific value (Fig. 2b), being consistent with that the effects of speed ratios are only valid within a certain range [42].

4.3. *Strain homogeneity improvement with the ASR processing*

One advantage of the ASR process relative to the SR process is that it can effectively penetrate the plastic strain into the plate center and improve the homogeneity of the plastic strain distribution along ND, as shown in Fig. 3 and Table 1. Roumina and Sinclair [42] pointed out that the shear strain can be introduced into the plate by speed mismatch, and thus the central equivalent plastic strain could be increased. During the ASR process, the cross-shear region (CSR) between two neutral points is considered to be the major difference compared to the SR process, which is also the critical region where the rolling force is reduced and the shear strain is introduced into the center [45,54]. It is not enough to explain how the plastic strains are accumulated along with improved through-thickness homogeneity, but which can be explained by the appearance of through-thickness HSRB during the ASR processing. The HSRBs are symmetrically generated for the SR process at the upper and bottom surfaces and transmitted into the plate center, where both parts are counteracted. As a result, the HSRBs are weakened without accumulating shear strains at the center part. For the ASR process with asymmetrical HSRBs at the upper and lower surface layers, the stronger HSRBs generated from the lower surface can go through the plate thickness. Moreover, a second through-thickness HSRB may occur at higher i and larger Δh, and also can go through the plate thickness without being affected or annihilated by the HSRB generated at the opposite side. This widely distributed through-thickness HSRB could help improving the homogeneity of strain distribution and the accumulation of the plastic strain at the center layer. According to Dhinwal and Toth [55], the deformation path can be divided into two stages: the compressive strains are mainly accumulated in the first stage near the biting region and the shear strains are mainly accumulated in the second stage. Other FE researches also observed shear bands in the latter part of the deformation zone, which located roughly at the same position as the present through-thickness HSRB [3,36]. Therefore, with the enhanced through-thickness HSRB, the ASR process could effectively introduce the shear strains into the plate center and improve the through-thickness strain homogeneity.

5. Conclusions

This study aims at in-depth understanding of the deformation mechanism during the ASR processing of the (mid-)thick aluminium alloy plates and determining where the strains occur and accumulate. It shows that the bending amplitude and direction occurred during the ASR processing are obviously affected by rolling parameters, i.e., increasing the speed ratio will facilitate the upward bending under the same Δh but it is opposite with increasing Δh under the same i. The equivalent plastic strain level can be increased with larger Δh while its distribution along ND is affected by the speed ratios.

The plastic strains are mainly accumulated at the HSRBs with their distribution, intensity and transfer direction depending on the ASR parameters, which will subsequently affect the strain distribution and curvature amplitude/direction. These findings can pave a fundamental way for understanding the deformation behavior and optimizing multi-pass asymmetric rolling processes for the (mid-)thick aluminium alloy plates and other metallic alloy plates.

CRediT authorship contribution statement

Hui Su: Conceptualization, Data curation, Formal analysis, Methodology, Investigation, Writing - Original draft. **Longgang Hou:** Conceptualization, Supervision, Writing - Review & Editing, Visualization, Funding acquisition. **Qingkun Tian:** Investigation, Data curation. **Yawen Wang:** Investigation, Data curation, Validation. **Linzhong Zhuang:** Supervision, Writing - Review & Editing, Funding acquisition.

Declaration of competing interest

The authors declare that they have no known competing financial interests or personal relationships that could have appeared to influence the work reported in this paper.

Acknowledgement

The authors are grateful for the financial supports from the Constructed Project for Key Laboratory of Beijing, China [No. BJSJ2019004], and the State Key Laboratory for Advanced Metals and Materials of China [No. 2018Z-23]. L. H. and L. Z. also acknowledge the supports from CHINALCO.

REFERENCES

[1] Ma B, Li C, Wang J, Cai B, Sui F. Influence of asymmetric hot rolling on through-thickness microstructure gradient of Fe-20Mn-4Al-0.3C non-magnetic steel. Mater Sci & Eng A 2016;671:190–7.
[2] Han ZH, Liang S, Yang J, Wei R, Zhang CJ. A superior combination of strength-ductility in CoCrFeNiMn high-entropy alloy induced by asymmetric rolling and subsequent annealing treatment. Mater Char 2018;145:619–26.
[3] Li C, Ma B, Song Y, Zheng J, Wang J. Grain refinement of non-magnetic austenitic steels during asymmetrical hot rolling process. J Mater Sci Technol 2017;33(12):1572–6.
[4] Angella G, Jahromi BE, Vedani M. A comparison between equal channel angular pressing and asymmetric rolling of silver in the severe plastic deformation regime. Mater Sci & Eng A 2013;559:742–50.
[5] Ji YH, Park JJ. Development of severe plastic deformation by various asymmetric rolling processes. Mater Sci & Eng A 2009;499(1–2):14–7.
[6] Yang J, Li S, Liu L, Li X, Zhang X. Finite element analysis of bending behavior and strain heterogeneity in snake rolling of AA7050 plates using a hyperbolic sine-type constitutive law. J Mater Process Technol 2017;240:274–83.
[7] Kim WJ, Lee KE, Choi S-H. Mechanical properties and microstructure of ultra fine-grained copper prepared by a high-speed-ratio differential speed rolling. Mater Sci & Eng A 2009;506(1–2):71–9.
[8] Uniwersał A, Wróbel M, Wierzbanowski K, Wroński D, Baczmański A. Mechanical and microstructural characteristics of polycrystalline copperrolled asymmetrically to a high deformation level. Mater Char 2019;148:214–23.
[9] Ren X, Huang Y, Zhang X, Li H, Zhao Y. Influence of shear deformation during asymmetric rolling on the microstructure, texture, and mechanical properties of the AZ31B magnesium alloy sheet. Mater Sci & Eng A 2021;800:140306.
[10] Ko YG, Hamad K. Structural features and mechanical properties of AZ31 Mg alloy warm-deformed by differential speed rolling. J Alloys Compd 2018;744:96–103.
[11] Ji YH, Park JJ, Kim WJ. Finite element analysis of severe deformation in Mg-3Al-1Zn sheets through differential-speed rolling with a high speed ratio. Mater Sci & Eng A 2007;454–455:570–4.
[12] Cho JH, Kim HW, Kang SB, Han TS. Bending behavior, and evolution of texture and microstructure during differential speed warm rolling of AZ31B magnesium alloys. Acta Mater 2011;59(14):5638–51.
[13] Xu Z, Zhang H, Krishnan P, Hale C, Kecskes LJ, Yarmolenko S, et al. Non-conventional hot rolling for improvement of mechanical properties in binary Mg-alloys. Mech Mater 2022;164:104111.
[14] Kim WJ, Hwang BG, Lee MJ, Park YB. Effect of speed-ratio on microstructure and mechanical properties of Mg-3Al-1Zn alloy in differential speed rolling. J Alloys Compd 2011;509(34):8510–7.
[15] Yang HW, Widiantara IP, Ko YG. Effect of deformation path on texture and tension properties of submicrocrystalline Al-Mg-Si alloy fabricated by differential speed rolling. Mater Lett 2018;213:54–7.
[16] Ko YG, Chaudry UM, Hamad K. Microstructure and mechanical properties of AA6061 alloy deformed by differential speed rolling. Mater Lett 2020;259:126870.
[17] Kraner J, Fajfar P, Palkowski H, Kugler G, Godec M, Paulin I. Microstructure and texture evolution with relation to mechanical properties of compared symmetrically and asymmetrically cold rolled aluminum alloy. Metals 2020;10(2):156.
[18] Wronski S, Bacroix B. Microstructure evolution and grain refinement in asymmetrically rolled aluminium. Acta Mater 2014;76:404–12.
[19] Kang JH, Ko YG. Microstructure and mechanical properties of ultrafine grained 5052 Al alloy fabricated by multi-pass differential speed rolling. J Mater Res Technol 2022;19:2031–49.
[20] Ko YG, Hamad K. Microstructure stability and mechanical properties of ultrafine grained 5052 Al alloy fabricated by differential speed rolling. Mater Sci & Eng A 2018;733:24–7.
[21] Polkowski W, Jóźwik P, Polański M, Bojar Z. Microstructure and texture evolution of copper processed by differential speed rolling with various speed asymmetry coefficient. Mater Sci & Eng A 2013;564:289–97.
[22] Tamimi S, Gracio JJ, Lopes AB, Ahzi S, Barlat F. Asymmetric rolling of interstitial free steel sheets: microstructural evolution and mechanical properties. J Manuf Process 2018;31:583–92.
[23] Wu Y, Zhang Z, Zhang Y, Kong C, Yu H. Twinning susceptibility of CrCoNi medium entropy alloy to cryogenic temperature during asymmetric rolling. J Mater Res Technol 2022;20:2638–49.
[24] Ko YG, Kim YG, Hamad K. Microstructure optimization of low-carbon steel using differential speed rolling deformation followed by annealing. Mater Lett 2020;261:127154.
[25] Qian T, Marx M, Schüler K, Hockauf M, Vehoff H. Plastic deformation mechanism of ultra-fine-grained AA6063 processed by equal-channel angular pressing. Acta Mater 2010;58(6):2112–23.
[26] Liu Y, Lu C, Wang H, Tieu AK, Liu B. Microstructure evolution, lattice rotation retardation and grain orientation fragmentation in commercial purity aluminium deformed by high pressure torsion. J Mater Res Technol 2020;9(3):6642–54.
[27] Kamikawa N, Sakai T, Tsuji N. Effect of redundant shear strain on microstructure and texture evolution during accumulative roll-bonding in ultralow carbon IF steel. Acta Mater 2007;55(17):5873–88.
[28] Wang Q, Ebrahimi M. Accumulative roll-bonding of aluminum alloys and composites: an overview of properties and performance. J Mater Res Technol 2022;19:4381–403.
[29] Anders D, Münkerb T, Artelb J, Weinberg K. A dimensional analysis of front-end bending in plate rolling applications. J Mater Process Technol 2012;212(6):1387–98.
[30] Nilsson A. Front - end bending in plate rolling. Scand J Metall 2001;30:337–44.

[31] Lu JS, Harrer OK, Schwenzfeier W, Fischer FD. Analysis of the bending of the rolling material in asymmetrical sheet rolling. Int J Mech Sci 2000;42(1):49–61.
[32] Markowski J, Dyja H, Knapiński M, Kawałek A. Theoretical analysis of the asymmetric rolling of sheets on leader and finishing stands. J Mater Process Technol 2003;138(1–3):183–8.
[33] Son RC, Sim KH,OSH. FE Simulation of the influence of roll diameter difference on the plate curvature during hot plate rolling. Steel Res Int 2018;90(4):1800007.
[34] Knight CW, Hardy SJ, Lees AW, Brown KJ. Investigations into the influence of asymmetric factors and rolling parameters on strip curvature during hot rolling. J Mater Process Technol 2003;134(2):180–9.
[35] Qwamizadeh M, Kadkhodaei M, Salimi M. Asymmetrical sheet rolling analysis and evaluation of developed curvature. Int J Adv Manuf Technol 2012;61:227–35.
[36] Sui FL, Wang X, Zhao J, Ma B, Li CS. Analysis on shear deformation for high manganese austenite steel during hot asymmetrical rolling process using finite element method. J of Iron & Steel Res Int. 2015;22(11):990–5.
[37] Dong H, Guo F, Huang W, Yang X, Zhu X, Li H, et al. Shear banding behavior of AA2099 Al-Li alloy in asymmetrical rolling and its effect on recrystallization in subsequent annealing. Mater Char 2021;177:111155.
[38] Chang LL, Kang SB, Cho JH. Influence of strain path on the microstructure evolution and mechanical properties in AM31 magnesium alloy sheets processed by differential speed rolling. Mater Des 2013;44:144–8.
[39] Taali S, Moazzen P, Toroghinejad MR. Annealing texture in asymmetrically rolled $Ni_{1.5}FeCrCu_{0.5}$ high-entropy alloy. J Mater Res Technol 2022;18:5075–86.
[40] Xiao B, Song J, Tang A, Jiang B, Sun W, Liu Q, et al. Effect of pass reduction on distribution of shear bands and mechanical properties of AZ31B alloy sheets prepared by online heating rolling. J Mater Process Technol 2020;280:116611.
[41] Hamad K, Park JH, Ko YG. Finite element analysis of deformation behavior in Al-2.2 wt. % Mg alloy subjected to differential speed rolling. J Mater Eng Perform 2015;24(8):2990–3001.
[42] Ma R, Lu Y, Wang L, Wang Y. Influence of rolling route on microstructure and mechanical properties of AZ31 magnesium alloy during asymmetric reduction rolling. Trans Nonferrous Metals Soc China 2018;28(5):902–11.
[43] Wang J, Liu X, Sun X. Study on asymmetrical cold rolling considered sticking friction. J Mater Res Technol 2020;9(6):14131–41.
[44] Tzou GY. Relationship between frictional coefficient and frictional factor in asymmetrical sheet rolling. J Mater Process Technol 1999;86(1–3):271–7.
[45] Wang J, Liu X, Sun X. Study on the relationship between asymmetrical rolling deformation zone configuration and rolling parameters. Int J Mech Sci 2020;187:105905.
[46] Shore D, Kestens LAI, Sidor J, Houtte PV, Bael AV. Process parameter influence on texture heterogeneityin asymmetric rolling of aluminium sheet alloys. Int J Material Form 2018;11:297–309.
[47] Amegadzie MY, Bishop DP. Effect of asymmetric rolling on the microstructure and mechanical properties of wrought 6061 aluminum. Mater Today Commun 2020;25:101283.
[48] Ma C, Hou L, Zhang J, Zhuang L. Influence of thickness reduction per pass on strain, microstructures and properties of 7050 Al alloy sheet processed by asymmetric rolling. Mater Sci & Eng A 2016;650:454–68.
[49] Li S, Qin N, Liu J, Zhang X. Microstructure, texture and mechanical properties of AA1060 aluminum. Mater Des 2016;90:1010–7.
[50] Pawelski H. Comparison of methods for calculating the influence of asymmetry in strip and plate rolling. Steel Res 2000;71(12):490–6.
[51] Kasai D, Komori A, Ishii A, Yamada K, Ogawa S. Strip warpage behavior and mechanism in single roll driven rolling. ISIJ Int 2016;56(10):1815–24.
[52] Kawałek A. Forming of band curvature in asymmetrical rolling process. J Mater Process Technol 2004;155–156:2033–8.
[53] Gao H, Ramalingama SC, Barbera GC, Chen G. Analysis of asymmetrical cold rolling with varying coefficients of friction. J Mater Process Technol 2002;124(1–2):178–82.
[54] Zhang SH, Zhao DW, Gao CR, Wang GD. Analysis of asymmetrical sheet rolling by slab method. Int J Mech Sci 2012;65(1):168–76.
[55] Dhinwal SS, Toth LS. Unlocking deformation path in asymmetric rolling by texture simulation. Materials 2020;13(1):101.